


# Photoconductive heaters enable control of large-scale silicon photonic ring resonator circuits

HASITHA JAYATILLEKA,<sup>1,2,†,\*</sup>  HOSSAM SHOMAN,<sup>1,†</sup>  LUKAS CHROSTOWSKI,<sup>1</sup> AND SUDIP SHEKHAR<sup>1</sup>

<sup>1</sup>Department of Electrical and Computer Engineering, University of British Columbia, 2332 Main Mall, Vancouver, British Columbia V6T 1Z4, Canada

<sup>2</sup>Current address: Intel Corporation, 2200 Mission College Blvd, Santa Clara, California 95054, USA

\*Corresponding author: hasitha@ece.ubc.ca

Received 24 August 2018; revised 8 November 2018; accepted 21 December 2018 (Doc. ID 343150); published 15 January 2019

A multitude of large-scale silicon photonic systems based on ring resonators have been envisioned for applications ranging from biomedical sensing to quantum computing and machine learning. Yet, due to the lack of a scalable solution for controlling ring resonators, practical demonstrations have been limited to systems with only a few rings. Here, we demonstrate that large systems can be controlled by using only doped waveguide elements inside their rings while preserving their area and cost. We measure the large photoconductive changes of the waveguides for monitoring the rings' resonance conditions across high-dynamic ranges and leverage their thermo-optic effects for tuning. This allows us to control ring resonators without requiring additional components, complex tuning algorithms, or additional electrical I/Os. We demonstrate automatic resonance alignment of 31 rings of a  $16 \times 16$  switch and of a 14-ring coupled resonator optical waveguide, making them the largest, yet most compact, automatically controlled silicon ring resonator circuits to date, to the best of our knowledge. © 2019 Optical Society of America under the terms of the OSA Open Access Publishing Agreement

<https://doi.org/10.1364/OPTICA.6.000084>

## 1. INTRODUCTION

The miniature size of silicon ring resonators makes them attractive candidates for large-scale photonic systems, as they can be densely integrated on-chip for lowering size, power consumption, and cost [1–3]. As a result, numerous solutions based on ring resonators have been proposed for applications in communications systems [2,4–6], signal processing [1,7], quantum computing [8], sensing [9], and machine learning [10]. A key requirement for the practical use of these systems is the ability to precisely control the resonance conditions of their ring resonators, which allows to (1) correct for fabrication errors, (2) adapt the system in real time to account for temperature variations or laser wavelength fluctuations, and (3) reprogram the system altogether for implementing various transfer functions and different functionalities. Such control can be enabled by utilizing feedback loops to monitor and tune/track the resonance conditions of the rings until the desired conditions are met. Prior art for controlling ring resonators has depended on numerous photodetectors (PDs) for monitoring the rings' resonance conditions and on separate thermo/electro-optic phase shifters for tuning the rings [11–16]. However, these extra components often need additional processing steps (e.g., Ge depositions [14,17] or Si<sup>+</sup> implantations [18] for PD), increase the number of electrical inputs/outputs to the system, and occupy significantly large on-chip real estate [11,13–15]. Therefore, a low-cost single element that can be placed inside the resonator for monitoring and

tuning its resonance would be a true enabler for controlling large-scale systems.

In this paper, we discuss the physics, report on the photodetection quantum efficiencies (QEs), and demonstrate the capabilities of such a control element in tuning large-scale silicon ring resonator systems. The control element we demonstrate is based on a doped silicon nanowire waveguide, which is ubiquitously found across many industrial silicon photonics platforms without additional process modifications. We combine the doped waveguides' photoconductive effects together with their thermo-optic tuning capabilities for monitoring and tracking the ring resonators' resonance conditions, respectively. Previously, we used similar doped waveguides for controlling single- and coupled-ring resonators [19,20]. Yet, the scalability of such solutions towards large systems was unclear due to the unknown detection capabilities such as QEs and dynamic ranges. Here, we demonstrate capabilities of our photoconductive heaters, to the best of our knowledge, by automatically aligning the resonances of the largest number of rings on a silicon chip, i.e., 31 rings along the longest path of a  $16 \times 16$  switch and a 14-ring coupled resonator optical waveguide (CROW), respectively. While these systems show large insertion loss variations, the precise resonance detection is enabled by the large ( $> 43$  dB) dynamic range permitted by the record-high photoconductive QE of the doped waveguides. Almost all ring-resonator-based systems are formed by using two types of

circuits as building blocks: (1) rings interconnected through bus waveguides [1,4–6,10,21] and/or (2) rings coupled to each other (i.e., CROWs) [8,9,20,22,23]. In this paper, by demonstrating the automatic control of the largest number of resonators in each type of circuit, we show how such photoconductive heaters can be readily deployed to control a majority of the ring resonator systems proposed before.

The rest of this paper is organized as follows. In Section 2, we discuss the photoconductive and thermo-optic behaviors of the doped silicon waveguides demonstrating their high QEs, large dynamic ranges, photodetection bandwidths, and thermo-optic tuning bandwidths. We then show how they can be integrated into ring resonators for monitoring and tracking the rings' resonance conditions. In Section 3, we demonstrate tuning the ring resonators along the longest path of a  $16 \times 16$  switch, routing light through 31 ring resonators connected through bus waveguides and 30 waveguide crossings. In Section 4, we demonstrate the automatic resonance alignment of a CROW with 14 ring resonators.

## 2. SILICON WAVEGUIDE PHOTOCONDUCTIVE HEATERS

### A. Photoconductive and Thermo-Optic Behaviors of Doped Waveguides

Figure 1(a) illustrates the photoconductive mechanism of the doped silicon nanowire rib waveguides used in this work. In contrast to previous reports [13,18,24,25], the key enabler in our design is the lightly  $n$ -doped ( $5 \times 10^{17} \text{ cm}^{-3}$ ) waveguide core. In previous reports on silicon waveguide PDs, the waveguide was left undoped [24,25] or was implanted with  $\text{Si}^+$  ions [13,18], which either reduced the measurable photocurrent or increased the loss of the waveguide, respectively. Furthermore, a vast majority of previous reports relied on  $\text{pn}$ -junctions [13,18,26] for measuring photocurrents, which limited their use as phase tuners due to sub-nm tuning ranges. In our design, we use only  $n$ -type doping. While the doping in the waveguide core is low enough to allow for low-loss (doping loss = 5 dB/cm) propagation, it is sufficient enough to (1) lower the electrical resistance across the waveguide enabling the device to function as a thermo-optic tuner over appreciable wavelength ranges with low voltages compatible with CMOS circuitry and to (2) increase the measurable photocurrent to micro-amperes (for micro-watt input optical powers)

allowing the device also to function as a precise power monitor inside an optical circuit. We attribute the generation of the initial electron–hole pairs (EHPs) inside the waveguide to absorption in the small number of defect (due to doping) and surface states. As a result of the mobility difference between electrons and holes, electrons reach the positive terminal before holes reach the negative terminal (Fig. 1). Additional electrons are injected into the device from the negative terminal to maintain the semiconductor's charge neutrality and, hence, multiple electrons traverse across the device in the time it takes a photo-generated hole to reach the negative terminal. As a result, the number of collected electrons across the terminals far exceeds the number of photo-generated EHPs, resulting in a high photoconductive gain in the QE, yielding appreciable photocurrents with low loss.

Figure 2(a) shows the measured photocurrent ( $I_{\text{PD}}$ ) and QE for a 100  $\mu\text{m}$  long  $n$ -type photoconductive heater at an input power and wavelength of 10  $\mu\text{W}$  and 1.55  $\mu\text{m}$ , respectively, as a function of the applied heater bias ( $V_{\text{heater}}$ ). First, the dark current ( $I_{\text{heater}}$ ) was measured with the input laser turned off [see Supplement 1, Fig. S2(c)].  $I_{\text{PD}}$  was then obtained by subtracting the calibrated  $I_{\text{heater}}$  from the total measured current when the input laser was on. When calculating QE, we estimated the total insertion loss of the device to be 0.069 dB, arising from a doping loss of 5 dB/cm and a scattering loss of 1.9 dB/cm. Therefore, the QE reported here represents the smallest possible QE (see Supplement 1, Section 2). In Fig. 2(a), the QE peaks to 64 at 1.4 V and starts to diminish for higher bias voltages. This is because the difference between electron and hole mobilities diminishes at high fields, reducing the photoconductive gain [27]. Figure 2(b) shows the measured photocurrents, and Fig. 2(c) shows the corresponding QEs as functions of the optical power entering a similar device at a bias of 1 V. The QE reduces for high optical powers due to the saturation of the defect and surface states in the waveguide. Figure 2(b) shows detection of optical powers ranging from  $-35 \text{ dBm}$  to  $8 \text{ dBm}$  across a 43 dB dynamic range. The measurable dynamic range here was limited by the largest input optical power and smallest measurable  $I_{\text{PD}}$  allowed by our setup. The smallest measurable  $I_{\text{PD}}$  was limited due to the measurement error of our source-measure unit, where we estimated the standard deviation  $\sigma$  value to be 0.15  $\mu\text{A}$  when measured at a bias of 1 V over an integration time of 416.7 ms per measurement. In the experiments described in Sections 3 and

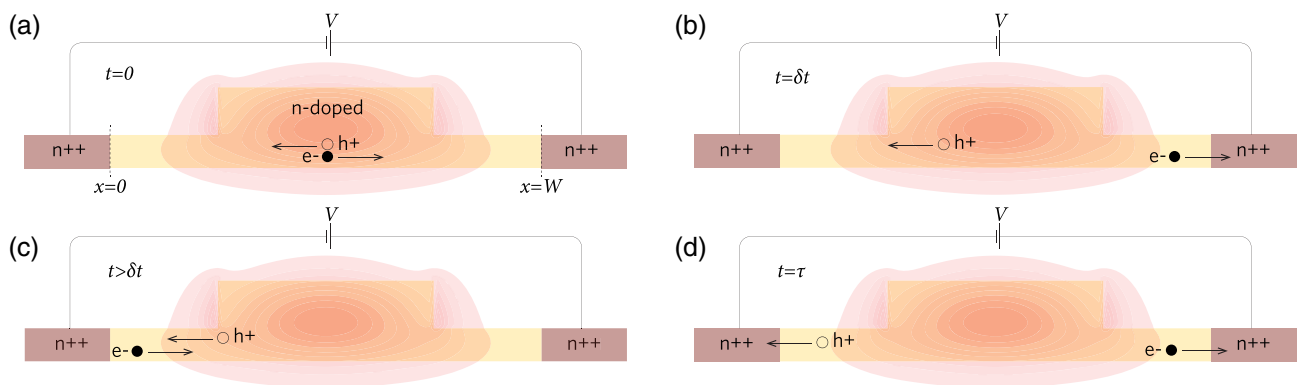


**Fig. 1.** Photoconductivity of a silicon nanowire waveguide. Cross sections of a silicon waveguide illustrating the transport of a photogenerated electron and hole towards the terminals at different velocities. The additional electrons injected from the negative terminal in order to maintain the charge neutrality of the semiconductor result in a large net gain in the QE. The center of the waveguide is lightly doped ( $5 \times 10^{17} \text{ cm}^{-3}$ ), whereas the sides are highly doped to form ohmic contacts. The overlap of the simulated TE optical mode at 1.55  $\mu\text{m}$  with the waveguide is also shown.

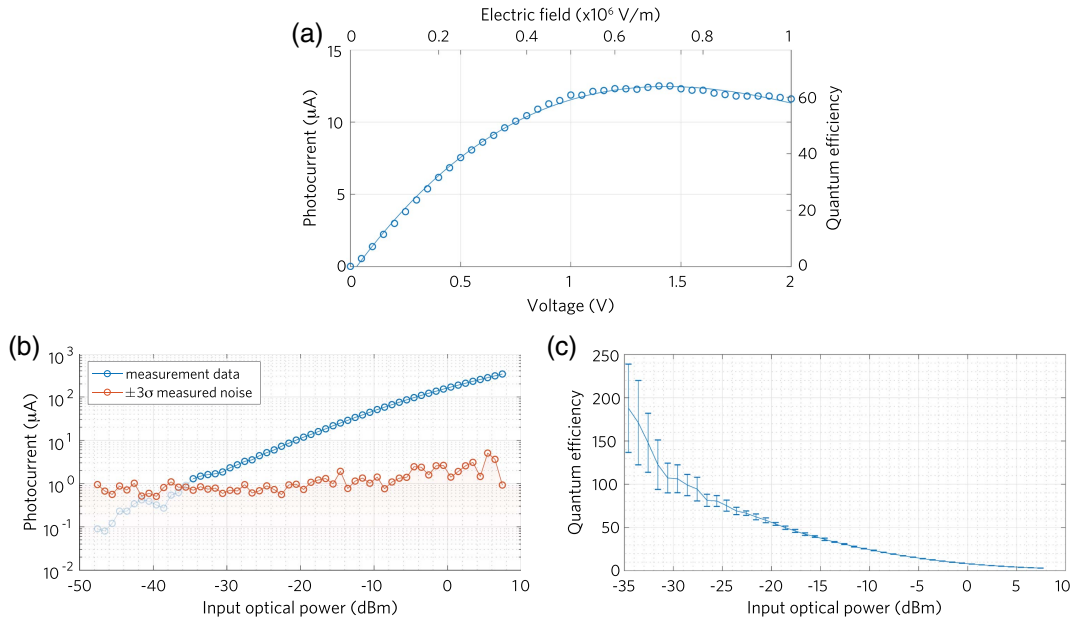


**Fig. 2.** Photoconductivity response of a silicon nanowire waveguide. Photocurrent and QE measured from a 100  $\mu\text{m}$  long photoconductive waveguide as functions of the (a) bias voltage (at an input power of 10  $\mu\text{W}$ ). The large gain in QE reduces beyond 1.4 V due to the electrons and holes reaching their respective saturation velocities. The solid line is a polynomial fit to the measurement. Measured (b) photocurrent and (c) QE as functions of the input optical power (at a bias voltage of 1 V). In (b),  $\pm 3\sigma$  variation of the  $I_{\text{PD}}$  measurement at each input optical power is shown. In (c), the QE reduces with the input optical power due to saturation of the defect and surface states. The error bars shown in (c) correspond to the error in QE due to the  $\pm 3\sigma$  current measurement noise.

4, we used an integration time of 16.7 ms for photocurrent measurement. The  $\sigma$  value for each optical input power was calculated from 50 photocurrent measurements [see Supplement 1, Fig. S2(d) for  $\sigma$  calculation of the dark current  $I_{\text{heater}}$ ]. In Fig. 2(b), we set the noise floor to  $\pm 3\sigma$  (0.9  $\mu\text{A}$ ) for reporting photocurrents and QE values.

A photoconductive heater's detection bandwidth depends on the electron and hole transit times across the waveguide. Figure 3(a) shows the dynamic response of a photoconductive heater measured by modulating the input light with a 500 kHz square wave. We extracted the rise and fall times and the 3 dB photodetection bandwidth [28] of the device to be 0.28  $\mu\text{s}$  and 570 kHz, respectively. Figure 3(b) shows the dynamic thermo-optic response measured by modulating a similar photoconductive heater embedded in a Mach-Zehnder interferometer with a 100 kHz square wave voltage signal. The 3 dB thermo-optic tun-

ing bandwidth was extracted to be 175 kHz. As the 3 dB photodetection bandwidth is much greater than the thermo-optic bandwidth, loop bandwidth of a feedback-based ring resonance tracking system using integrated CMOS electronic circuits will likely be limited by the thermo-optic tuning speed.

## B. Ring Resonator Control

Figure 4(a) shows the integration of a photoconductive heater into a silicon ring resonator of 8  $\mu\text{m}$  radius by n-doping a quarter of the ring's perimeter. The ring's intracavity optical power can be measured (via  $I_{\text{PD}}$ ), and the resonance can be tuned (via  $I_{\text{heater}}$ ) using this single element. The same contact pad is used for measuring  $I_{\text{PD}}$  and supplying the heater current,  $I_{\text{heater}}$ , for tuning. Therefore, additional electrical I/Os are not necessary to fully control the ring by using a feedback loop for sensing and tuning its resonance. Figure 4(b) shows the measured drop-port

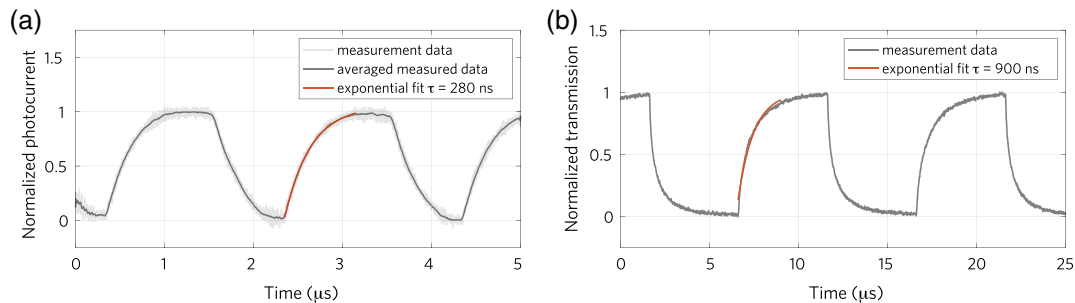


**Fig. 3.** Time-domain photodetection and thermo-optic tuning responses of a photoconductive heater. (a) Photodetection response of the device heater when the input light is modulated at 500 kHz. The rise time of the response is 0.28  $\mu\text{s}$ , corresponding to a photodetection bandwidth of 570 kHz. (b) Thermo-optic response of the photoconductive heater measured by modulating a device integrated into a Mach-Zehnder interferometer with a 100 kHz square wave signal. The rise time of the response is 0.9  $\mu\text{s}$ , corresponding to a 3 dB thermo-optic tuning bandwidth of 175 kHz.

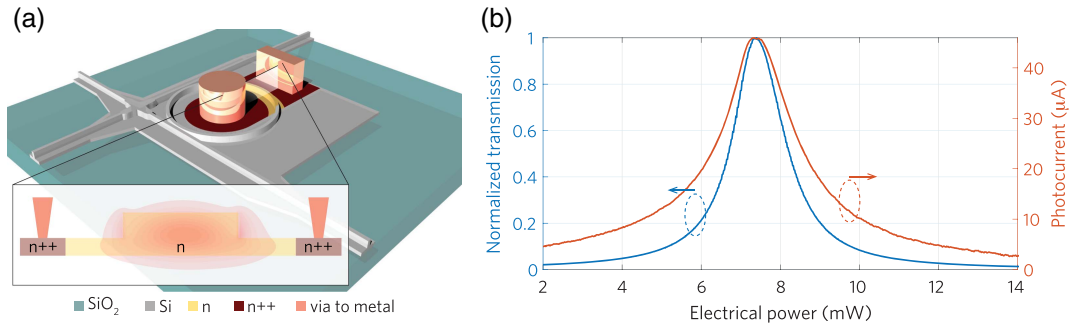


**Fig. 4.** Integrated photoconductive heaters in a silicon ring resonator. (a) Illustration of a photoconductive heater integrated into the ring resonator with 8  $\mu\text{m}$  radius (drawn to scale). The top  $\text{SiO}_2$  cladding is not shown. The inset shows an overlap of the simulated TE optical mode at 1.55  $\mu\text{m}$  in the bent waveguide. (b) Measured drop-port transmission (left axis) and photocurrent from the photoconductive heater (right axis) of the ring as a function of the supplied electrical power to the heater. The ring can be set to be resonant with the input light by maximizing the photocurrent.

transmission and photocurrent,  $I_{\text{PD}}$ , as a function of the supplied electrical power to the heater. The electrical power to the heater is controlled by setting the heater voltage  $V_{\text{heater}}$ . As compared to a straight waveguide, the photocurrent measured from the ring is further amplified due to the energy build-up inside the cavity. Both the drop-port transmission, which is proportional to the ring's intracavity optical power, and the measured  $I_{\text{PD}}$  change in sync with each other, and they are both maximized at the same electrical power. Hence, the ring can be set to be resonant with the input laser's wavelength by maximizing the photocurrent,  $I_{\text{PD}}$ . If the resonator's bandwidth is extremely narrow, behavior of photoconductivity as a function of the heater voltage,  $V_{\text{heater}}$ , [see Fig. 2(a)] can introduce a deviation between the  $V_{\text{heater}}$  values that maximize the drop-port response and  $I_{\text{PD}}$ . In such cases, the measured  $I_{\text{PD}}$  values can be calibrated to account for the change in photoconductivity as a function of the heater's voltage [see Fig. 2(a)]. Due to the large optical pass bandwidths (e.g., 3 dB bandwidth of the resonator shown in Fig. 4 is 44 GHz) of the resonators used in this work, we did not observe any appreciable deviation between  $V_{\text{heater}}$  values that maximized the drop-port response and  $I_{\text{PD}}$ . In addition,  $I_{\text{PD}}$  is also temperature dependent. However, maximum seeking algorithms used in this work can overcome such a level shift in  $I_{\text{PD}}$  caused by a temperature drift that is much slower than the tracking speed. In a previous work, we demonstrated tracking the response of a four-ring CROW across a 65°C temperature variation [20].

The ring resonator shown in Fig. 4(a) requires 48 mW for tuning across the 12.1 nm free spectral range (FSR). In a commercial application, this tuning power can be further reduced by about an order of magnitude by selective silicon substrate removal techniques [29]. While the intrinsic  $Q$ -factor of this ring is limited to about  $1.4 \times 10^5$  due to the light doping, the doping concentration or the length of the doped portion in the ring can be traded off in applications requiring higher  $Q$ -factors. The length of the photoconductive heater in the ring is chosen to be 12.55  $\mu\text{m}$  to allow for thermo-optic tuning across the entire FSR within the supply voltage range. The lower limit for the ring resonator's radius for avoiding excessive bending losses for the waveguide geometry (Fig. 1) is about 8  $\mu\text{m}$  [30].

### 3. TUNING OF SWITCH MATRIX

Ring resonator-based switches are attractive for applications in data centers and in high-performance computers due to their

promise for high-speed switching, small footprints, and low power consumption [1,2,6]. Here, by programming the rings of a  $16 \times 16$  silicon ring-resonator-based switch, we demonstrate the automatic programming of a large system where the rings are interconnected via bus waveguides. Figure 5(a) shows a microscope picture of the fabricated switch. The  $16 \times 16$  switch consists of 256 unit cells arranged in a cross-grid [1,31] packed into a compact area of 6.11  $\text{mm}^2$ . In comparison, an  $8 \times 8$  switch based on Mach-Zehnder interferometers occupied 8.25  $\text{mm}^2$  in prior art [32]. Our design can be made further compact by shrinking the contact pads, here designed to be 80  $\mu\text{m} \times 80 \mu\text{m}$  for ease of prototyping. Figure 5(b) shows a microscope picture of a unit cell. The 8  $\mu\text{m}$  radius ring resonator and waveguide crossing used in the unit cell is similar to that illustrated in Fig. 4.

In order to demonstrate that we can automatically route any input port to any cross/bar-port, we chose to automatically align the resonances of the 31 rings along the longest route of the switch (labeled as diagonal in Fig. 5) from input-port  $I_1$  to cross-port  $C_{16}$ . This was accomplished by sequentially tuning the rings along the diagonal, starting from the ring nearest to the input port to maximize the photocurrent in each ring. Before tuning, the dark current or the heater current,  $I_{\text{heater}}$ , was measured and recorded for all the heaters in the voltage range of interest. As described previously, during the tuning process, the monitor photocurrent  $I_{\text{PD}}$  of each ring was measured by subtracting the calibrated  $I_{\text{heater}}$  from the total current measured. Limited by our measurement setup (see Supplement 1, Section 3), we tuned only one ring at a time, and the voltages of the previously tuned rings were held constant. When rings 8, 16, 24, and 31 along the diagonal path were reached, we repeated the tuning starting from ring 1 to adjust for any detunings due to thermal and electrical crosstalk. In an industrial application, this re-tuning can be avoided by continuously seeking the maximum photocurrents in the rings simultaneously. It is important to note that in our system, the feedback loop controlling each ring is local to itself. Therefore, when tuning all of the rings simultaneously, each ring's control circuit detects and corrects for any deviation of its resonance from the channel wavelength, including any perturbations due to thermal crosstalk from surrounding heat sources. Hence, this approach can be readily scaled to systems with any number of rings, as long as there is sufficient light inside the rings for accurately sensing their resonance conditions.



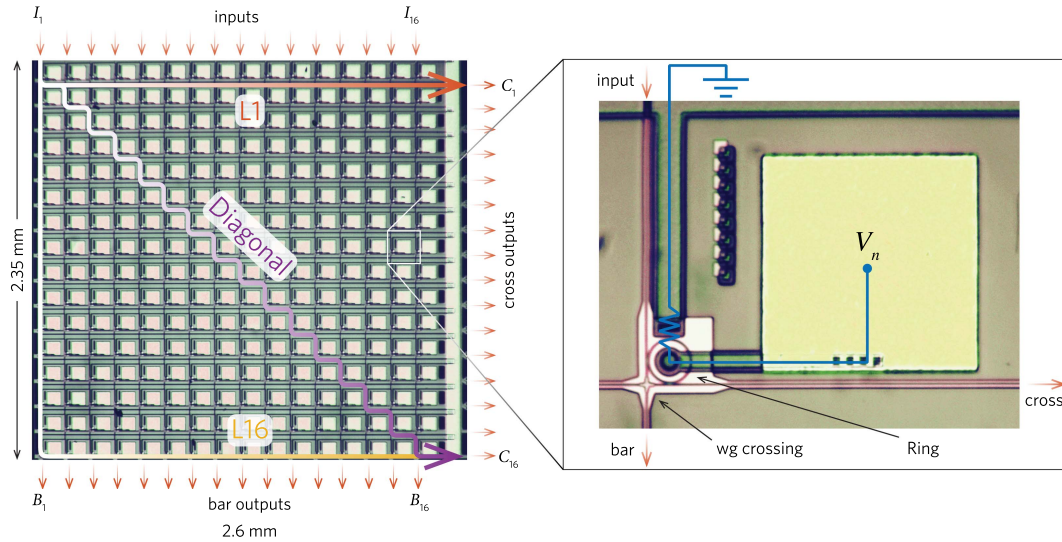


**Fig. 5.**  $16 \times 16$  ring resonator switch. Microscope picture of the fabricated switch showing the inputs ( $I_1 - I_{16}$ ), and bar ( $B_1 - B_{16}$ ) and cross ( $C_1 - C_{16}$ ) outputs. The three routing configurations demonstrated in this paper are indicated as diagonal,  $L_1$ , and  $L_{16}$ . The inset shows the microscope picture of a unit cell. The location of the photoconductive heater is shown as a resistor in the circuit.

Figures 6(a) and 6(b) show the maximum photocurrents measured in each ring and the heater powers required for tuning the 31 rings of the diagonal route from port  $I_1$  to  $C_{16}$ . The total power consumption of the rings after tuning was 212 mW. Figure 6(c) shows the measured spectral response from port  $I_1$  to  $C_{16}$  as fabricated (blue) and after tuning the diagonal route (purple). Figure 6(c) also shows the spectral responses measured by routing light via routes  $L_1$  and  $L_{16}$ . Configuring paths  $L_1$  and  $L_{16}$  required tuning only a single resonator to be resonant with the channel wavelength. Using these measurements, we estimated the insertion loss of a single ring and a crossing to be 0.3 dB and 0.4 dB, respectively (see Supplement 1, Fig. S5). The diagonal route, which routed light through 30 crossings and 31 rings, suffered the highest insertion loss. In the future, these losses can be

reduced by design improvements [33]. In fact, the high insertion loss further indicates the capability of our photoconductive heaters in accurately measuring optical powers across a dynamic range exceeding 21.3 dB, where the input powers to the first and last rings in the path were estimated to be 7.2 dBm and -14.1 dBm, respectively. As shown in Fig. 6(c), the simulated transmission spectra of the diagonal including the insertion loss of the rings and crossings agree well near the peak wavelength with the measured spectral response. The mismatch away from the peak wavelength is caused by the parasitic pathways formed through untuned rings of the system, which increased the optical power collected away from the peak wavelength in the experiment. Light in such parasitic pathways can be minimized by tuning the rings not belonging to the light path away (turned off) from their

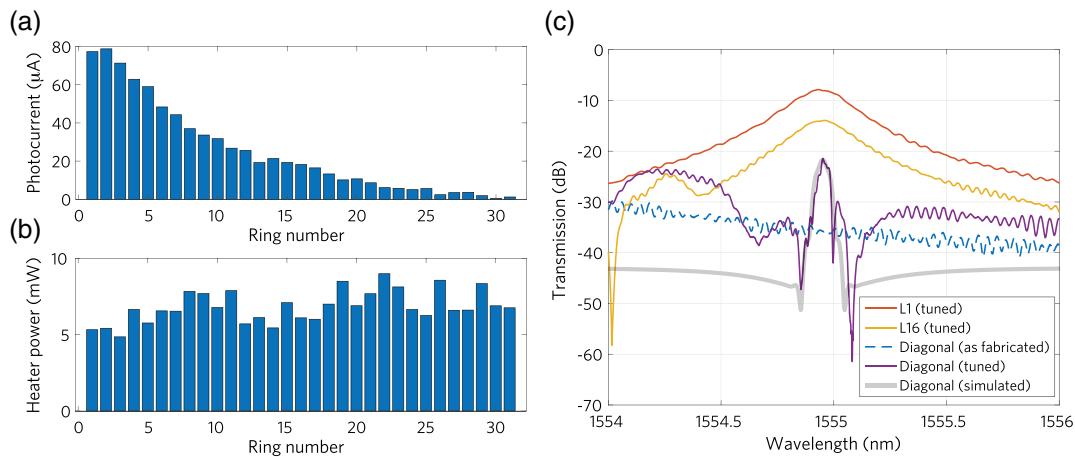


**Fig. 6.** Programming the switch. (a) Maximum photocurrent measured in each ring's photoconductive heater when tuning the 31 rings along the diagonal from  $I_1$  to  $C_{16}$ . (b) Corresponding electrical powers supplied to the heaters that maximize the photocurrents. (c) Measured spectral responses for the as-fabricated and the after-configured switch along  $L_1$ ,  $L_{16}$ , and diagonal paths. The simulated transfer function for the diagonal agrees well with the measured response near the peak wavelength. However, a mismatch exists away from the peak wavelength. This is because in simulation, we assumed that all of the rings not in the diagonal were tuned away from the peak wavelength by half of the FSR (i.e., turned off). However, in the experiment, the resonances of these rings were not controlled and the parasitic pathways formed through these rings increased the optical power collected away from the peak wavelength.

resonances. The simulated result for the diagonal path in Fig. 6(c) shows this case, where we have assumed that all of the rings not in the diagonal were tuned away from the peak wavelength by half of the FSR (i.e., turned off).

#### 4. TUNING OF 14-RING CROW

Coupling ring resonators to form CROWs is an attractive approach for designing devices such as optical filters with flat pass-bands and steep roll-offs, optical delay lines, and four-wave mixing elements for a range of applications from sensing to quantum computing [8,9,23]. Due to the coupling between their rings, resonance conditions of the rings of a CROW cannot be readily determined from its outputs alone. In this work, by embedding photoconductive heaters into each of the rings of a CROW, we directly probe the rings' intracavity powers to find the desired resonance conditions using a simple tuning technique. We demonstrate automatic resonance alignment of a 14-ring CROW, correcting for the unwanted resonance shifts of its rings due to fabrication variations. Figure 7(a) shows a microscope picture of the fabricated 14-ring CROW. The inset illustrates the integration of photoconductive heaters into each of the rings. The rings, starting from the ring coupled to the input port, are denoted as  $R_1$  through  $R_{14}$ . The ring-ring and ring-bus waveguide couplings were chosen for a maximally flat drop-port response (see Supplement 1, Section 1). The area occupied by the 14 rings and their photoconductive heaters is only  $13.5 \times 10^3 \mu\text{m}^2$ .

In order to automatically tune the CROW to the input laser's wavelength, first, we tuned rings  $R_1$  through  $R_{14}$  to maximize the

photocurrent in each ring's photoconductive heater. This step brought the resonances of all the rings closer to the input laser's wavelength, which ensured that sufficient photocurrent could be detected in each ring for the subsequent tuning steps. Next, we tuned the rings in reverse order from  $R_{14}$  through  $R_1$ . During each tuning step, while tuning the  $n$ th ring ( $R_n$ ), we measured photocurrents of rings  $R_{n-1}$  and  $R_n$ . The heater power corresponding to the desired resonance condition of  $R_n$  was found by maximizing the ratio of the photocurrents  $I_{\text{PD},n}/I_{\text{PD},n-1}$ , where  $I_{\text{PD},n}$  is the photocurrent measured in the  $n$ th ring [20]. When  $R_1$  was reached, we maximized  $I_{\text{PD},1}$  to find its resonance condition. (Supplement 1, Fig. S6, shows the measured photocurrents and their ratios  $I_{\text{PD},n}/I_{\text{PD},n-1}$  for these 14 tuning steps). Finally, we iterated over these 14 tuning steps several times in order to adjust for any undesired detunings due to the thermal crosstalk between the rings. In simulation, we verified that the desired solution could be reached by iterating the tuning steps in the above described sequence. For example, detuning due to ambient temperature changes can be corrected by continuously cycling through the tuning steps. The feedback loops used here for finding the resonance conditions of the rings are local to the adjacent rings of the CROW, i.e., the desired resonance condition of a ring can be found only by sensing a ring and its neighbor without knowing/sensing the resonance conditions of the other rings of the CROW. Hence, this localization paves the path towards tuning CROWs with even higher numbers of rings by minimizing the requirement of a "supervisory" control unit.

Figure 7(b) shows the as-fabricated through- and drop-port responses of the CROW, and Fig. 7(c) shows the improved responses after tuning. While the theoretically simulated extinction

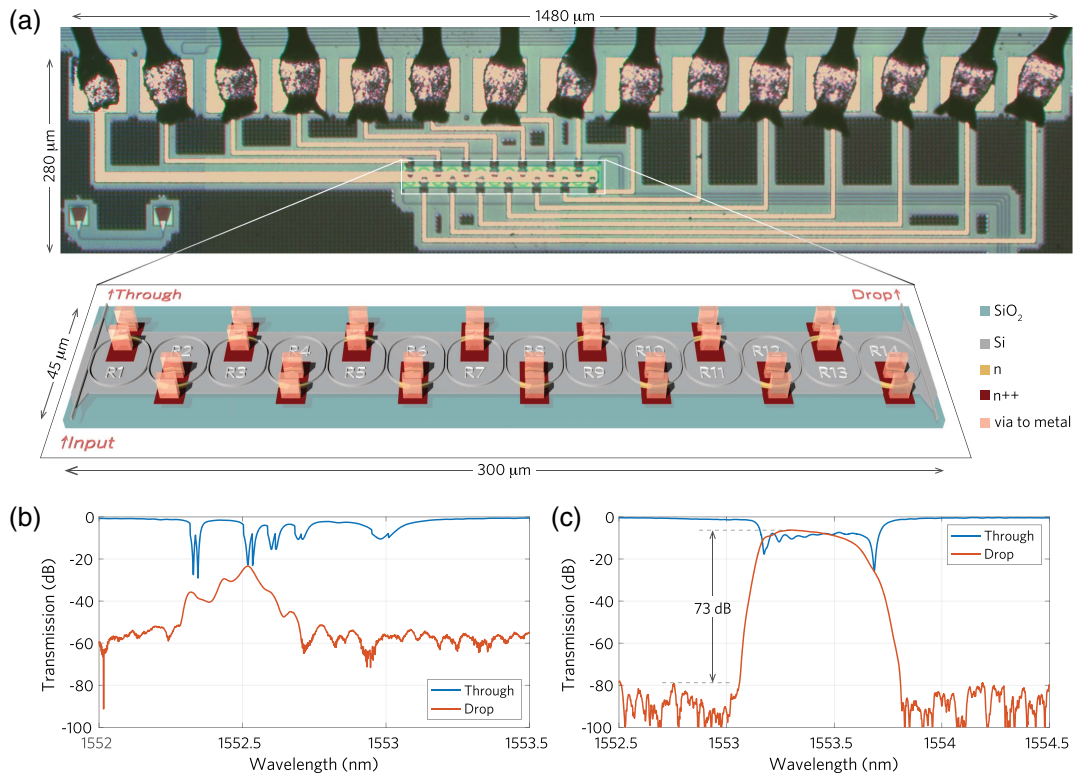


**Fig. 7.** Resonance alignment of 14-ring CROW. (a) Microscope picture of the fabricated 14-ring CROW. The inset illustrates the layout of photoconductive heaters in the rings. (b) Measured as-fabricated through- and drop-port spectra of the CROW. (c) Measured through- and drop-port spectra after tuning.

ratio of this device exceeds 200 dB, the measurable extinction ratio here is about 73 dB due to limitations with the measurement instruments and the insertion loss of the grating couplers. The noise floor of the post-tuning spectra was reduced by averaging over 1000 consecutive spectral sweeps collected using the optical vector network analyzer [34]. After tuning, the 14 rings consumed total power of 64.9 mW. Insertion loss of the tuned CROW at the center of the drop-port pass-band was 7.15 dB. The FSR of the tuned filter was 8.4 nm at 1553.4 nm wavelength.

## 5. CONCLUSION

We showed record-high photoconductive QEs (up to 200) in doped silicon waveguides. Using such photoconductive heaters, we demonstrated the automatic alignment of 31 ring resonators along the longest path of a  $16 \times 16$  switch and the tuning of a 14-ring CROW. These are the largest, yet most compact, automatically tuned silicon ring resonator circuits to date. The high QE and the large dynamic range of the photoconductive heaters allowed the resonance conditions of individual resonators of these systems to be precisely sensed and tuned simultaneously without the need for additional material depositions (zero change to foundry fabrication process [35]), PDs, or complex tuning algorithms, and without increasing the number of contact pads. As a result of this increased insight into the resonance conditions of individual resonators of the system, the tuning methods we used localized the feedback loops to individual resonators of the switch and to the adjacent resonators of the CROW. Therefore, these methods are readily applicable for tuning a ring-resonator-based system regardless of the number of resonators, as long as there is sufficient light in each resonator for sensing the resonance conditions, i.e.,  $> -35$  dBm for the work presented here. By providing a highly scalable and a low-cost solution that preserves the miniature sizes of silicon ring resonators, our results indicate a path forward for making a multitude of long-promised ring resonator systems demonstrated in previous works over the past two decades viable in practice [1,4,6–10,21,23].

**Funding.** Natural Sciences and Engineering Research Council of Canada (NSERC) SiEPIC Program; CMC Microsystems.

**Acknowledgment.** The authors thank W. Bogaerts, N. A. F. Jaeger, A. Ribeiro, M. Hammood, and A. Park for their help, S. Shang of Testforce Systems for lending an optical vector analyzer, CMC microsystems for providing access to fabrication and design tools, and NSERC, the SiEPIC program, and CMC Microsystems for financial support.

See [Supplement 1](#) for supporting content.

<sup>†</sup>These authors contributed equally to this work.

## REFERENCES

- C. Batten, A. Joshi, J. Orcutt, A. Khilo, B. Moss, C. W. Holzwarth, M. A. Popovic, H. Li, H. I. Smith, J. L. Hoyt, F. X. Kartner, R. J. Ram, V. Stojanovic, and K. Asanovic, "Building many-core processor-to-DRAM networks with monolithic CMOS silicon photonics," *IEEE Micro* **29**, 8–21 (2009).
- Q. Cheng, S. Rumley, M. Bahadori, and K. Bergman, "Photonic switching in high performance datacenters [invited]," *Opt. Express* **26**, 16022–16043 (2018).
- P. Dong, A. Melikyan, and K. Kim, "Commercializing silicon microring resonators: technical challenges and potential solutions," in *Conference on Lasers and Electro-Optics* (Optical Society of America, 2018), paper SM4B.3.
- A. H. Atabaki, S. Moazeni, F. Pavanello, H. Gevorgyan, J. Notaros, L. Alloati, M. T. Wade, C. Sun, S. A. Kruger, H. Meng, K. Al Qubaisi, I. Wang, B. Zhang, A. Khilo, C. V. Baiocco, M. A. Popović, V. M. Stojanović, and R. J. Ram, "Integrating photonics with silicon nanoelectronics for the next generation of systems on a chip," *Nature* **556**, 349–354 (2018).
- P. Dong, Y. Chen, T. Gu, L. L. Buhl, D. T. Neilson, and J. H. Sinsky, "Reconfigurable 100 Gb/s silicon photonic network-on-chip," *J. Opt. Commun. Netw.* **7**, A37–A43 (2015).
- D. Nikolova, D. M. Calhoun, Y. Liu, S. Rumley, A. Novack, T. Baehr-Jones, M. Hochberg, and K. Bergman, "Modular architecture for fully non-blocking silicon photonic switch fabric," *Microsyst. Nanoeng.* **3**, 16071 (2017).
- A. Khilo, S. J. Spector, M. E. Grein, A. H. Nejadmalayeri, C. W. Holzwarth, M. Y. Sander, M. S. Dahlem, M. Y. Peng, M. W. Geis, N. A. DiLello, J. U. Yoon, A. Motamedi, J. S. Orcutt, J. P. Wang, C. M. Sorace-Agaskar, M. A. Popović, J. Sun, G.-R. Zhou, H. Byun, J. Chen, J. L. Hoyt, H. I. Smith, R. J. Ram, M. Perrott, T. M. Lyszczarz, E. P. Ippen, and F. X. Kärtner, "Photonic ADC: overcoming the bottleneck of electronic jitter," *Opt. Express* **20**, 4454–4469 (2012).
- R. Kumar, J. R. Ong, M. Savanier, and S. Mookherjee, "Controlling the spectrum of photons generated on a silicon nanophotonic chip," *Nat. Commun.* **5**, 5489 (2014).
- J. Wang, Z. Yao, T. Lei, and A. W. Poon, "Silicon coupled-resonator optical-waveguide-based biosensors using light-scattering pattern recognition with pixelized mode-field-intensity distributions," *Sci. Rep.* **4**, 7528 (2014).
- A. N. Tait, T. F. de Lima, E. Zhou, A. X. Wu, M. A. Nahmias, B. J. Shastri, and P. R. Prucnal, "Neuromorphic photonic networks using silicon photonic weight banks," *Sci. Rep.* **7**, 7430 (2017).
- K. Padmaraju and K. Bergman, "Resolving the thermal challenges for silicon microring resonator devices," *Nanophotonics* **3**, 269–281 (2014).
- Y. Zhang, Y. Li, S. Feng, and A. W. Poon, "Towards adaptively tuned silicon microring resonators for optical networks-on-chip applications," *IEEE J. Sel. Top. Quantum Electron.* **20**, 136–149 (2014).
- Y. Li and A. W. Poon, "Active resonance wavelength stabilization for silicon microring resonators with an in-resonator defect-state-absorption-based photodetector," *Opt. Express* **23**, 360–372 (2015).
- J. C. C. Mak, W. D. Sacher, T. Xue, J. C. Mikkelsen, Z. Yong, and J. K. S. Poon, "Automatic resonance alignment of high-order microring filters," *IEEE J. Quantum Electron.* **51**, 1–11 (2015).
- S. Grillanda, M. Carminati, F. Morichetti, P. Ciccarella, A. Annoni, G. Ferrari, M. Strain, M. Sorel, M. Sampietro, and A. Melloni, "Non-invasive monitoring and control in silicon photonics using CMOS integrated electronics," *Optica* **1**, 129–136 (2014).
- Z. Wang, D. Paez, A. I. A. El-Rahman, P. Wang, L. Dow, J. C. Cartledge, and A. P. Knights, "Resonance control of a silicon micro-ring resonator modulator under high-speed operation using the intrinsic defect-mediated photocurrent," *Opt. Express* **25**, 24827–24836 (2017).
- C. V. Poulton, P. Dong, and Y. K. Chen, "Photoresistive microring heater with resonance control loop," in *Conference on Lasers and Electro-Optics (CLEO)* (2015), paper SM2I.3.
- M. W. Geis, S. J. Spector, M. E. Grein, J. U. Yoon, D. M. Lennon, and T. M. Lyszczarz, "Silicon waveguide infrared photodiodes with  $>35$  GHz bandwidth and phototransistors with 50 AW-1 response," *Opt. Express* **17**, 5193–5204 (2009).
- H. Jayatilika, K. Murray, M. Á. Guillén-Torres, M. Caverley, R. Hu, N. A. F. Jaeger, L. Chrostowski, and S. Shekhar, "Wavelength tuning and stabilization of microring-based filters using silicon in-resonator photoconductive heaters," *Opt. Express* **23**, 25084–25097 (2015).
- H. Jayatilika, H. Shoman, R. Boeck, N. A. F. Jaeger, L. Chrostowski, and S. Shekhar, "Automatic configuration and wavelength locking of coupled silicon ring resonators," *J. Lightwave Technol.* **36**, 210–218 (2018).
- A. S. Khope, T. Hirokawa, A. M. Netherton, M. Saeidi, Y. Xia, N. Volet, C. Schow, R. Helkey, L. Theogarajan, A. A. Saleh, J. E. Bowers, and R. C. Alfemess, "On-chip wavelength locking for photonic switches," *Opt. Lett.* **42**, 4934–4937 (2017).

22. D. Aguiar, M. Milanizadeh, E. Guglielmi, F. Zanetto, R. Ji, S. Zhou, Y. Li, X. Song, L. Zhang, M. Sampietro, F. Morichetti, and A. Melloni, "Automatic tuning of microring-based hitless reconfigurable add-drop filters," in *Optical Fiber Communications Conference and Exposition (OFC)* (2018).
23. F. Morichetti, C. Ferrari, A. Canciamilla, and A. Melloni, "The first decade of coupled resonator optical waveguides: bringing slow light to applications," *Laser Photon. Rev.* **6**, 74–96 (2012).
24. L. Zhou, H. Zhu, H. Zhang, and J. Chen, "Photoconductive effect on p-i-p micro-heaters integrated in silicon microring resonators," *Opt. Express* **22**, 2141–2149 (2014).
25. T. Baehr-Jones, M. Hochberg, and A. Scherer, "Photodetection in silicon beyond the band edge with surface states," *Opt. Express* **16**, 1659–1668 (2008).
26. Q. Zhang, H. Yu, T. Qi, Z. Fu, X. Jiang, and J. Yang, "Enhancing bulk defect-mediated absorption in silicon waveguides by doping compensation technique," *Sci. Rep.* **8**, 9929 (2018).
27. S. O. Kasap, *Optoelectronics and Photonics: Principles and Practices* (Prentice Hall, 2013).
28. M. R. Watts, W. A. Zortman, D. C. Trotter, G. N. Nielson, D. L. Luck, and R. W. Young, "Adiabatic resonant microrings (arms) with directly integrated thermal microphotronics," in *Conference on Lasers and Electro-Optics and 2009 Conference on Quantum Electronics and Laser Science (CLEO/QELS)* (IEEE, 2009).
29. P. Dong, W. Qian, H. Liang, R. Shafiiha, D. Feng, G. Li, J. E. Cunningham, A. V. Krishnamoorthy, and M. Asghari, "Thermally tunable silicon racetrack resonators with ultralow tuning power," *Opt. Express* **18**, 20298–20304 (2010).
30. H. Jayatileka, K. Murray, M. Caverley, N. A. Jaeger, L. Chrostowski, and S. Shekhar, "Crosstalk in SOI microring resonator-based filters," *J. Lightwave. Technol.* **34**, 2886–2896 (2016).
31. A. W. Poon, X. Luo, F. Xu, and H. Chen, "Cascaded microresonator-based matrix switch for silicon on-chip optical interconnection," *Proc. IEEE* **97**, 1216–1238 (2009).
32. A. Annoni, E. Guglielmi, M. Carminati, S. Grillanda, P. Ciccarella, G. Ferrari, M. Sorel, M. J. Strain, M. Sampietro, A. Melloni, and F. Morichetti, "Automated routing and control of silicon photonic switch fabrics," *IEEE J. Sel. Top. Quantum Electron.* **22**, 169–176 (2016).
33. D. Celo, P. Dumais, W. Liu, C. Zhang, D. J. Goodwill, J. Jiang, and E. Bernier, "Optical proximity correction in geometry sensitive silicon photonics waveguide crossings," in *14th IEEE International Conference on Group IV Photonics (GFP)* (2017).
34. J. R. Ong, R. Kumar, and S. Mookherjee, "Ultra-high-contrast and tunable-bandwidth filter using cascaded high-order silicon microring filters," *IEEE Photon. Technol. Lett.* **25**, 1543–1546 (2013).
35. "Fab: Advanced micro foundry (AMF) silicon photonics fabrication process," 2018, <https://www.cmc.ca/en/WhatWeOffer/Products/CMC-00200-03001.aspx>.



# Photoconductive heaters enable control of large-scale silicon photonic ring resonator circuits: supplementary material

HASITHA JAYATILLEKA<sup>1,2,3,\*</sup>, HOSSAM SHOMAN<sup>1,3,\*</sup>, LUKAS CHROSTOWSKI<sup>1</sup>, AND SUDIP SHEKHAR<sup>1</sup>

<sup>1</sup>Department of Electrical and Computer Engineering, University of British Columbia, 2332 Main Mall, Vancouver, British Columbia V6T 1Z4, Canada

<sup>2</sup>Currently with Intel Corporation, 2200 Mission College Blvd, Santa Clara, California, 95054, USA

<sup>3</sup>Contributed equally to this work

\*Corresponding author: hasitha@ece.ubc.ca, hoshoman@ece.ubc.ca

Published 15 January 2019

This document provides supplementary information to "Photoconductive heaters enable control of large-scale silicon photonic ring resonator circuits," <https://doi.org/10.1364/OPTICA.6.000084>. Details are provided about fabrication, design, and experimental procedures for the devices presented in the main article.

## 1. DEVICE DESIGN AND FABRICATION

The silicon rib nanowire waveguides were designed to be 500 nm-wide and 220 nm-high, with 90 nm-thick slab sections to the sides of the waveguide core (see Fig. 1 of paper). Photoconductive heaters were created by n-doping the center of the waveguides ( $5 \times 10^{17} \text{ cm}^{-3}$ ). The slab sections of the waveguides 500 nm away from the core were heavily doped to form ohmic contacts to the silicon. Fig. S2c shows a measured IV curve of 100  $\mu\text{m}$  long photoconductive heater. The resistance of the device at 1 V is 1.3 k $\Omega$ .

The switch's ring resonators were designed to have a radius of 8  $\mu\text{m}$ . The bus-to-ring gaps were chosen to be 200 nm for all of the rings. The photoconductive heater occupied 25% of the microring's circumference (12.55  $\mu\text{m}$ ). The ground connections of all 256 photoconductive heaters were connected together. The input and cross-ports of the switch corresponding to several selected routes were connected to grating couplers to facilitate optical inputs and outputs. The switch's ring resonators were arranged in a square grid with a spacing of 150  $\mu\text{m}$  between the adjacent rings. The spacing can be further reduced by decreasing the footprint of the contact pads. Reducing the spacing between the rings can increase the amount of thermal crosstalk. We measured the detuning of a ring due to crosstalk heating from a ring located 100  $\mu\text{m}$  away to be about 2.5 pm/mW dissipated by the aggressor (only two rings were activated with the victim and aggressors dissipating 5 mW and 20 mW, respectively).

In the CROW, circumference of each ring was 66.83  $\mu\text{m}$  with a circular section of radius 10  $\mu\text{m}$  and a straight

coupling section of 2  $\mu\text{m}$ . The coupling gaps between the bus-waveguides and the rings were chosen to be 200, 400, 475, 510, 520, 526, 528, 530, 528, 526, 520, 510, 475, 400, and 200 nm for a flat-top passband transmission and a wide bandwidth. Fig. S1 shows the simulated response of the filter. The coupling between waveguides was simulated using the finite difference time domain (FDTD) method. The overall response was then computed using the transfer matrix method. In each ring, the photoconductive heater occupied 10.47  $\mu\text{m}$  waveguide section. The doped sections were defined to be on the opposite sides of the adjacent rings in order to minimize the electrical crosstalk between their heaters. The entire device, including the contact pads and metal routing and pads occupied an area of 1480  $\mu\text{m} \times 280 \mu\text{m}$ . Grating couplers were used for optical inputs/outputs.

All of the devices were fabricated using 248 nm deep UV lithography in a silicon photonics processing line through Institute of Microelectronics (IME), A\*STAR, Singapore[1]. All the doping layers ( $n$  and  $n^{++}$ ) used in this work are standard to this processing line.

## 2. PHOTOCONDUCTIVITY MEASUREMENTS

The QE of the photoconductive heater can be calculated from,

$$\text{QE} = \frac{I_{\text{PD}}/q}{P_{\text{absorbed}}/h\nu}, \quad (\text{S1})$$

where  $q$  is the electron charge,  $h$  the Planck's constant and  $\nu$  the optical frequency. Optical power absorbed,  $P_{\text{absorbed}}$ , was calculated as  $P_{\text{absorbed}} = P_0(1 - e^{-\alpha l})$ , where  $P_0$  is the optical power

(in linear scale) going into the device,  $\alpha$  the propagation losses in photoconductive heater in  $\text{cm}^{-1}$ , and  $l$  the length of the doped waveguide in centimeters.  $P_0$  was calculated by measuring the response of loopback structure with grating couplers at  $1.55\ \mu\text{m}$  wavelength,  $P_{\text{GC}}$  (in dB). If the laser's input power is  $P_{\text{in}}$  (in dBm) then  $P_0 = P_{\text{in}} - P_{\text{GC}}/2$  (in dBm). The propagation loss of the doped waveguide sections ( $\alpha$ ) was measured by fitting the spectra of a similarly doped microring's response[2], where the doping losses were extracted to be about 5 dB/cm. The photoconductive heater's photodetection bandwidth was measured using the setup shown in Fig.S4b. The CW laser was internally modulated at 500 kHz generating a square signal with 50% duty cycle. A bias-T was used to bias the photoconductive heater and pass the AC photocurrent signal to an oscilloscope to display the temporal response of the photoconductive heater.

### 3. ELECTRO-OPTICAL SETUP FOR SWITCH AND CROW

The fabricated chips were assembled in an 84-pin Kyocera ceramic quad flat non-leaded chip carriers (PB-C86131). The devices were connected to the chip carriers via wirebonds. The chip carriers were placed in an 84-pin socket (AE11110-ND) and soldered to an FR-4 PCB. This PCB was placed on a 6-axis controlled stage, and connected to a source-measure circuit via jumper wires for electrical I/O. A fiber array with single mode polarization maintaining fibers was used to couple light into and out of the chip (See Fig.S3). Our source-measure circuit consisted of a 2 channel Keithley 2602 source measure unit (SMU), 64 voltage sources (by combining NI PXI-6704 and NI PXIe-6738), 2 Arduino Mega 2560 microcontrollers and in-house designed electrical switch board using MAX4053ACPE+ switch chips. The switchboard facilitated connecting either of the SMU channels or the voltage sources to the ring heaters as required. The Arduino boards supplied the digital logic to the switch board. A personal computer was used for controlling the SMU, voltage sources, and the switch board via the Arduinos. In the experiments presented in sections 3 and 4 of the paper, the output tuning voltages supplied to the rings were limited to a range of 0.1 V - 6.0 V. Fig.S4 shows a block diagram of this arrangement. We used a Keysight N7714A as the input light source for tuning. An Agilent 81682A tunable laser and a Keysight N7744A photodetector or an optical vector analyzer (Luna OVA 5000) were used to obtain the optical sweeps after tuning the  $16 \times 16$  switch and the 14-ring CROW.

### REFERENCES

1. "Fab: Advanced micro foundry (AMF) silicon photonics fabrication process," <https://www.cmc.ca/en/WhatWeOffer/Products/CMC-00200-03001.aspx>. Accessed: 2018-6-22.
2. M. Popović, *Theory and Design of High-index-contrast Micropotonic Circuits* (2008).

#### 4. SUPPLEMENTARY FIGURES

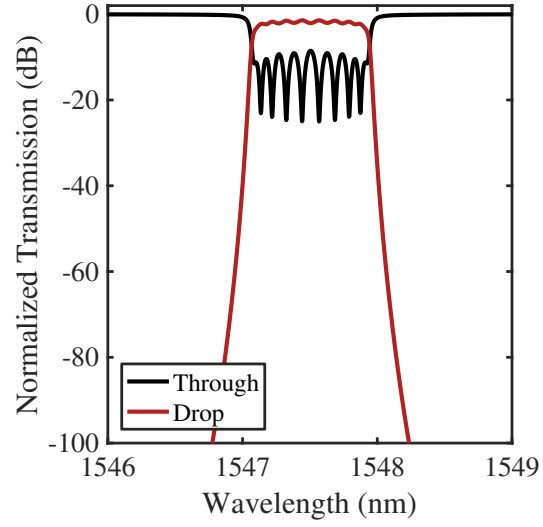


**Fig. S1.** Simulated response of the 14-Ring CROW as described in section S1. We attribute the mismatches between simulated and post-tuned response shown in Fig. 7c of the paper mainly to variation of the coupling gaps in fabrication. As the coupling sections are not tunable in this design, the deviations due to variations in coupling cannot be corrected post-fabrication by thermo-optic tuning.

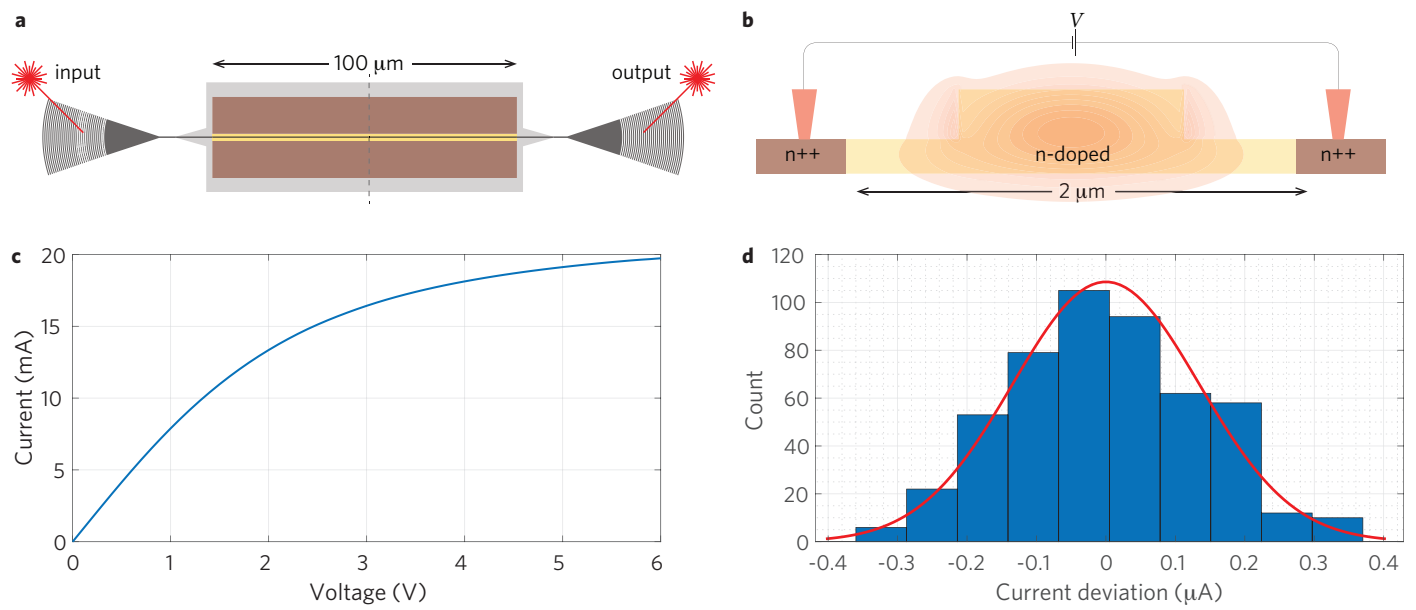


**Fig. S2.** Photoconductive heater used for QE measurements. (a) Layout top-view of the photoconductive heater used in the QE measurements. (b) Cross-section of the photoconductive heater. (c) Dark current of the photoconductive heater across the voltage applied to the heater's terminals. (d) 500 measurements of the dark current taken over 4 minutes. The standard deviation ( $\sigma$ ) is  $0.15\ \mu\text{s}$ .



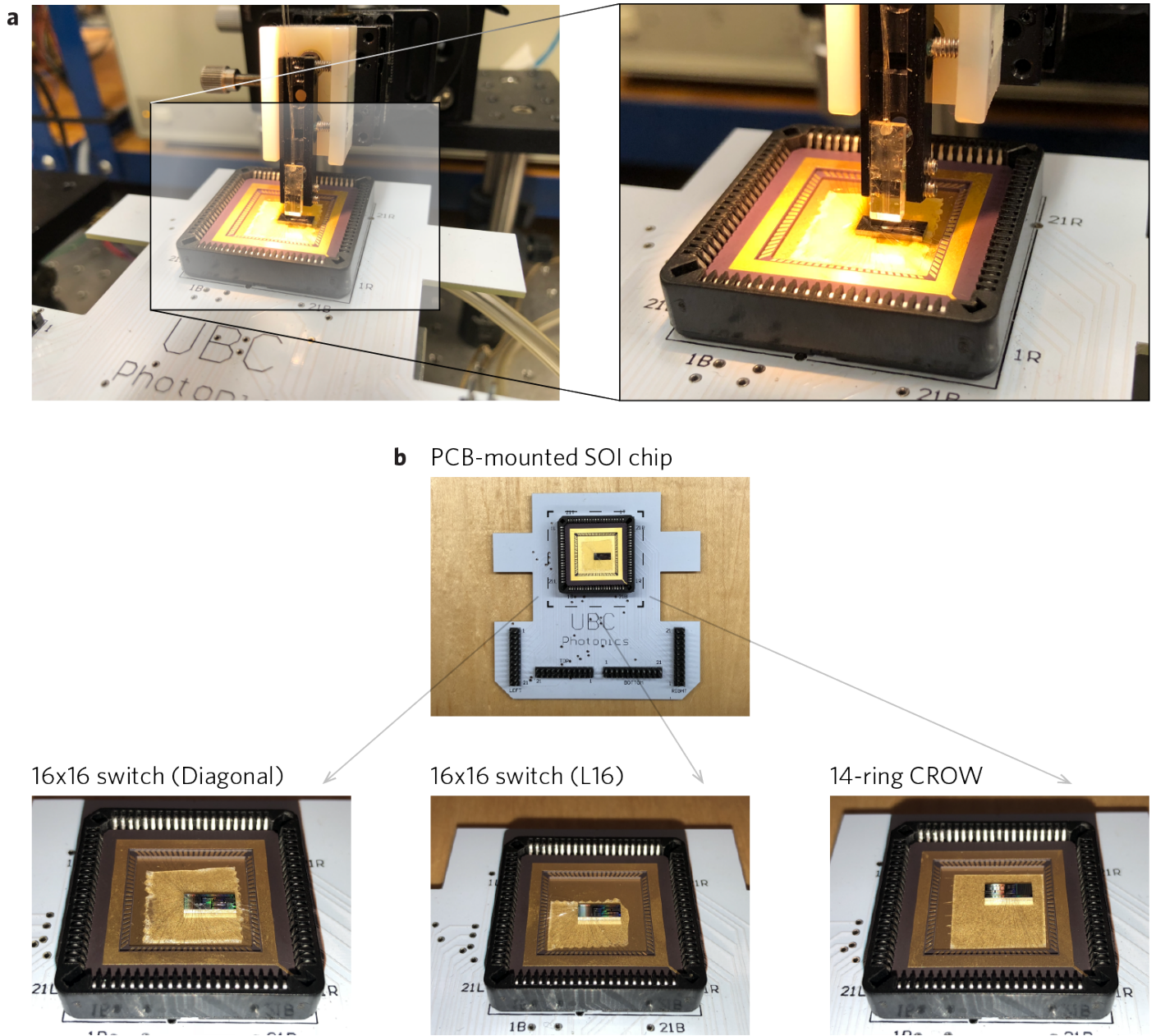


**Fig. S3.** Chip packaging for optical testing. (a) A fiber array with single mode polarization maintaining fibers was used to couple light into and out of the chips. The inset shows a zoomed-in view of the fiber array. The PCB shown is placed on a 6-axis controlled stage. (b) Top view of the fabricated chip assembled in an 84-pin Kyocera ceramic quad flat non-leaded chip carriers, placed in an 84-pin socket and soldered to an FR-4 PCB. The devices were connected to the chip carriers via wirebonds. The inset shows a close-up view of the wirebonded chips for each of the devices demonstrated in the paper: 1) the 16x16 switch for the diagonal case, 2) 16x16 switch for the L16 case, and 3) the 14-ring CROW.

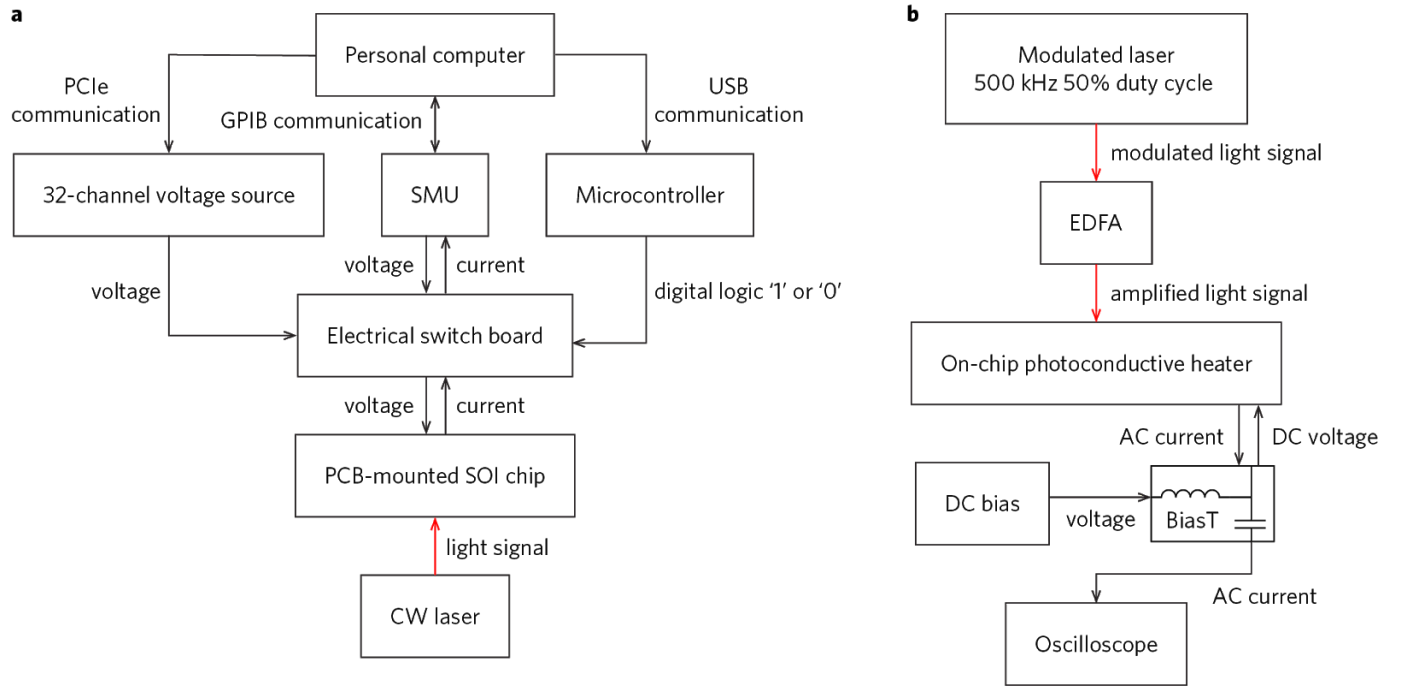


**Fig. S4.** Optical and electrical test setup configurations. (a) The block diagram of the setup used for tuning the 16x16 switch and the 14-ring CROW. The black and red lines indicate the electrical and optical signals, respectively. (b) The block diagram of the setup used to measure the temporal response of the photoconductive heater.

Table 1: Switch losses breakdown.

Path	Crossings	Rings	Total loss (dB)
$L_1 : I_1 \rightarrow C_1$	15	1	$\sim 8$
$L_{16} : I_1 \rightarrow C_{16}$	30	1	$\sim 14$
<b>Diagonal</b> : $I_1 \rightarrow C_{16}$	30	31	$\sim 21.5$

**Fig. S5.** Breakdown of the measured losses in each path of the switch.

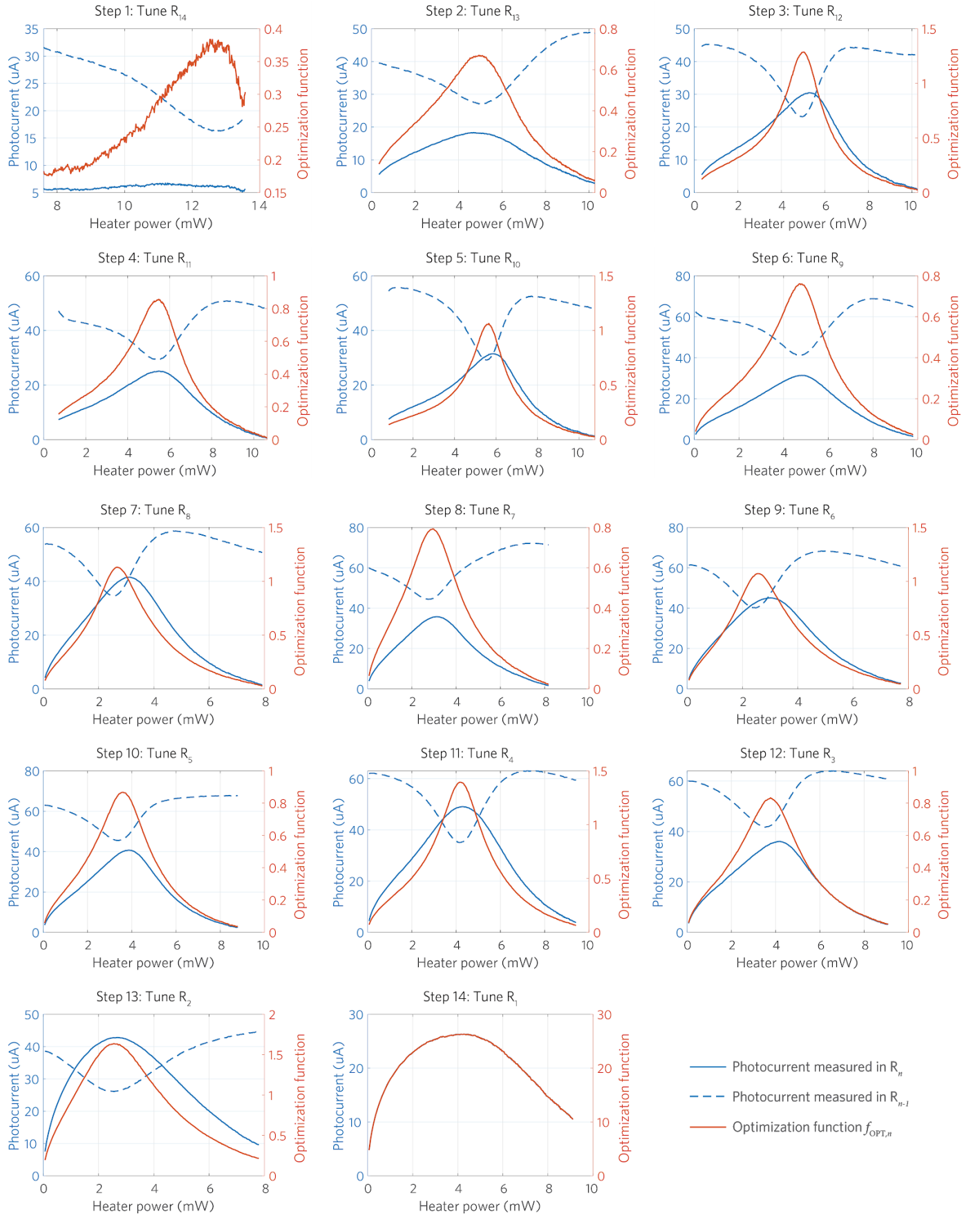


**Fig. S6.** Measured photocurrents and the optimization functions corresponding to each of the steps when tuning the 14-ring CROW. The rings  $R_{14}$ , which is coupled to the drop-port, through  $R_1$ , which is coupled to the through-port, were tuned. The optimization functions shown in the figures were calculated as  $I_{PD,n}/I_{PD,n-1}$ , where  $I_{PD,n}$  is the photocurrent measured in the  $n$ th ring. For the last ring tuned,  $R_1$ , the optimization function was its photocurrent  $I_{PD,1}$ . After each step, the voltages of the tuned ring  $R_n$ , was set to the voltage that maximized the optimization function.